Comput. Mech. (2006) 38: 482–490
DOI 10.1007/s00466-006-0065-6

ORIGINAL PAPER

Ryo Torii · Marie Oshima · Toshio Kobayashi
Kiyoshi Takagi · Tayfun E. Tezduyar

Fluid–structure interaction modeling of aneurysmal conditions with high and normal blood pressures

Received: 20 December 2005 / Accepted: 13 January 2006 / Published online: 13 May 2006

Abstract Hemodynamic factors like the wall shear stress play an important role in cardiovascular diseases. To investigate the influence of hemodynamic factors in blood vessels, the authors have developed a numerical fluid–structure interaction (FSI) analysis technique. The objective is to use numerical simulation as an effective tool to predict phenomena in a living human body. We applied the technique to a patient-specific arterial model, and with that we showed the effect of wall deformation on the WSS distribution. In this paper, we compute the interaction between the blood flow and the arterial wall for a patient-specific cerebral aneurysm with various hemodynamic conditions, such as hypertension. We particularly focus on the effects of hypertensive blood pressure on the interaction and the WSS, because hypertension is reported to be a risk factor in rupture of aneurysms. We also aim to show the possibility of FSI computations with hemodynamic conditions representing those risk factors in cardiovascular disease. The simulations show that the transient behavior of the interaction under hypertensive blood pressure is significantly different from the interaction under normal blood pressure. The transient behavior of the blood-flow velocity, and the resulting WSS and the mechanical stress in the aneurysmal wall, are significantly affected by hypertension. The results imply that hypertension affects the growth of an aneurysm and the damage in arterial tissues.

Keywords Cardiovascular modeling · Fluid–structure interaction · Patient-specific computation · Hypertension

1 Introduction

Computational hemodynamics has become a powerful and desirable tool in investigation of cardiovascular diseases [19] such as atherosclerosis and cerebral aneurysm, which are influenced by hemodynamic factors [3, 35, 15]. Measuring the hemodynamic factors such as the blood pressure and the wall shear stress (WSS) is still beyond the capabilities of in vivo measurement techniques. Image-based hemodynamic computations, embodied as fluid dynamics computations using patient-specific information for geometry and flow conditions, are expected to give us the capability to predict phenomena in human body. In fact, such hemodynamic computations have already been utilized in clinical setting [33].

Since cardiovascular diseases occur in vascular wall with stimulation by hemodynamic forces, and mass transfer of biological agents such as enzymes and proteins [9], multiphysics computations are expected to help us better understand the mechanisms of cardiovascular diseases. Advanced modeling techniques have enabled multi-physics computations to investigate hemodynamic and other factors contributing to disease progression. Arterial wall motion [14, 36], interaction between blood flow and arterial wall [20, 13] and mass transfer of atherogenetic substances [5, 12] were already taken into account. Fluid–structure interaction (FSI) simulations will particularly be helpful in investigating the cardiovascular diseases. This is because the WSS on the luminal wall and the mechanical stress in the vascular wall could be directly related to the location of the lesion [1, 32] and the blood flow strongly interacts with the vascular wall motion.

We have been investigating the hemodynamics [29, 11] and FSI [30] in the intracranial arteries using image-based computations to study the effects of hemodynamic factors

R. Torii (✉)
Department of Chemical Engineering, Imperial College,
South Kensington Campus, London SW7 2AZ, UK
E-mail: r.torii@imperial.ac.uk
Tel.: +44-20-75895111

M. Oshima
Institute of Industrial Science, The University of Tokyo,
4-6-1 Komaba, Meguro, Tokyo 153-8505, Japan

T. Kobayashi
Japan Automobile Research Institute, 2530 Karima,
Tsukuba, Ibaraki 305-0822, Japan

K. Takagi
Department of Neurosurgery, Ogura Hospital,
4-2-5 Nakamachi, Setagaya, Tokyo 158-8585, Japan

T. E. Tezduyar
Mechanical Engineering, Rice University — MS 321,
6100 Main Street, Houston, TX 77005, USA

on creation, progress and rupture of cerebral aneurysm. We showed the effects of the arterial geometry and the interaction between blood flow and arterial wall motion on hemodynamic factors. As a next step, we are applying various hemodynamic conditions to image-based FSI computations to investigate how those conditions affect the blood flow, the arterial motion, and the interaction between the two. By introducing various hemodynamic conditions representing the risk factors, which are typically derived from statistical studies [21], we also aim to show the potential of image-based computation as a risk-prediction tool for cardiovascular diseases. Because hypertension is one of the well known risk factors in subarachnoid hemorrhage (SAH) [21], we consider the hypertensive blood pressure condition in this study. Since over 95% of the SAH are caused by the rupture of cerebral aneurysm [7], hypertensive blood pressure can be regarded as a risk factor in rupture of cerebral aneurysm. We compute FSI with high and normal blood pressures and compare the results. We compare the results also to those obtained for rigid arterial walls at normal blood pressure. All these comparisons help us investigate the effect of hypertension on cerebral aneurysm.

2 Computational method

The blood flow in cerebral arteries is assumed to be laminar [6] and governed by the Navier–Stokes equations of incompressible flows. The fluid mechanics with moving walls is computed with the Deforming-Spatial-Domain /Stabilized Space–Time (DSD/SST) method [22, 25, 27]. In the DSD/SST formulation, the streamline-upwind /Petrov-Galerkin (SUPG) [2] and pressure-stabilizing/Petrov-Galerkin (PSPG) [22, 28] formulations are employed for stabilization. The DSD/SST method was developed for flows with moving boundaries and interfaces, and has been applied to a large class of problems [23, 24], including FSI [16–18].

The structural mechanics is governed by force equilibrium equation and computed with the Galerkin finite element method. The arterial wall is assumed to be made of linear elastic material and therefore a linear constitutive law is employed.

The fluid and structural mechanics systems are coupled at the interface by the kinematic and dynamic conditions. The two systems are solved with a block-iterative coupling approach. The fluid mesh is updated by using an automatic mesh moving method [26, 4], where the motion of the nodal points is governed by the equations of elasticity. The boundary conditions come from the motion of the interface between the fluid and structure. Details of computational method are described in [30].

3 Computational model

We constructed an arterial model with cerebral aneurysm based on computed tomography (CT). The model, which is shown in Fig. 1, is the left middle cerebral arterial (MCA) bifurcation. The patient is a 59-year-old female with a ruptured aneurysm. 150 CT slices with 0.60 mm interval were used for the geometry construction. Each CT slice consists of 512×512 pixels and were segmented with the region-growing scheme. The horizontal resolution of the CT slice is 0.3125 mm/pixel. The surface of the arterial lumen is then constructed with the marching-cubes method [8] as the iso-surface with the CT signal intensity. The construction process of the luminal surface was carried out with a commercial software ALATOVIEW. Since the arterial wall cannot be depicted in the CT but only the arterial lumen is depicted, the external wall of the artery in the computational model was constructed by expanding the luminal surface, assuming a uniform wall thickness of 0.3 mm. In Fig. 1b, the arterial wall is shown in red and the lumen is shown in light blue. The diameter of the arterial lumen is approximately 3 mm at the proximal end and 2 mm at the distal end. The diameter of the aneurysm is approximately 5 mm. Eight-noded hexahedral elements are used for the finite element discretization as shown in Fig. 1b. The meshes for the fluid and structural mechanics parts are made of 49,395 nodes and 46,000 elements and 11,520 nodes and 10,800 elements, resepectively. We employ first-order interpolation functions for all variables.

Although the blood is known to be non-Newtonian in general, we assume it to be Newtonian in this study. This is because we are focusing on large arteries with radii of

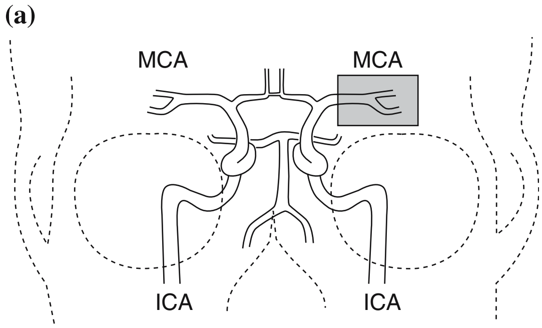

Cerebral arterial network.

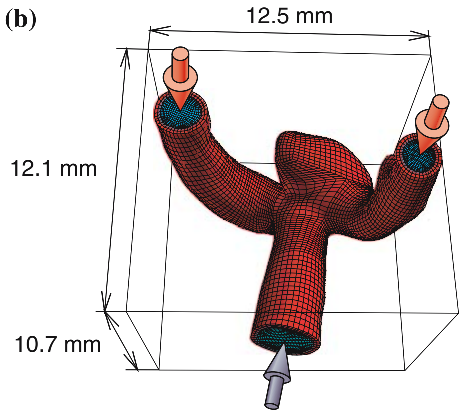

MCA model.

Fig. 1 Computational model

the order 1.0 mm, where the velocity and shear rate are high. The apparent viscosity is nearly constant when the shear rates are high [10]. The blood density and kinematic viscosity are specified as 1000 kg/m^3 and 4.0 m^2/s, respectively. The arterial wall is assumed to be made of linearly-elastic material. The elastic modulus and Poisson's ratio are set to 1.0 MPa and 0.49, respectively.

4 Boundary conditions and hypertension model

The inflow boundary condition, which is shown with the blue arrow in Fig. 1b, is a pulsatile velocity profile prescribed with the Womersley formulation [34]:

$$w(r,t) = \frac{2B_0}{\pi R^2}\left[1-\left(\frac{r}{R}\right)^2\right] + \sum_{n=1}^{N}\frac{B_n}{\pi R^2}\left[\frac{1-J_0\left(\alpha_n \frac{r}{R} i^{3/2}\right)/J_0\left(\alpha_n i^{3/2}\right)}{1-2J_1\left(\alpha_n i^{3/2}\right)/\left(\alpha_n i^{3/2} J_0\left(\alpha_n i^{3/2}\right)\right)}\right]e^{in\omega t}, \tag{1}$$

$$Q(t) = \sum_{n=0}^{N} B_n e^{in\omega t}, \tag{2}$$

where r is the cylindrical coordinate and t is time. R denotes the radius of the inlet cross section. Here J_0 and J_1 are Bessel functions of the first kind of order 0 and 1, and $\alpha_n = R\sqrt{n\omega/\nu}$, where ω is based on one cardiac cycle (=1.0 s). The non-dimensional parameter $\alpha = R\sqrt{\omega/\nu}$ is known as the Womersley number. The coefficients B_n are derived in reference to the velocity waveform measured with ultrasound Doppler velocimetry at the carotid artery of a healthy subject in his 20s. The flowrate waveform based on the measured velocity is shown in Fig. 2a with the red line, and the one computed with the Womersley profile is shown with the blue line. The resistance arising from the distal arterial networks are applied at the outflow boundaries as stress conditions, which are shown with the red arrows in Fig. 1b. The magnitude of the stress vector at the outlet, which corresponds to the outlet pressure, varies in time and is governed by following equation:

$$P(t) = \sum_{n=0}^{N} P_n e^{in\omega t}. \tag{3}$$

Here the coefficients P_n are determined, in an ad hoc fashion, based on B_n in the flowrate waveform to make the range of the variation within the standard blood pressure range of a healthy male, 80–120 mmHg. This means that the inflow velocity and the outlet pressure vary in the same phase. The resulting pressure waveform is shown in Fig. 2b. The blue and red lines depict the pressure waveform for the normal blood pressure (NBP) and high blood pressure (HBP) cases, respectively. No-slip condition is applied at the arterial wall.

In the structural mechanics computations, the hemodynamic force at the interface between the blood and arterial wall is used as the surface force. All ends of the artery are held fixed by specifying zero-displacement boundary conditions. The initial displacements and stresses are set to zero.

To investigate the effect of high blood pressure on the flow field, the motion of the arterial wall, and the interaction between the two, a hypertensive blood pressure condition is applied as the stress condition at the outflow boundary, with a variation range of 100–170 mmHg. The transient behavior of the HBP condition is shown in Fig. 2b with the red line.

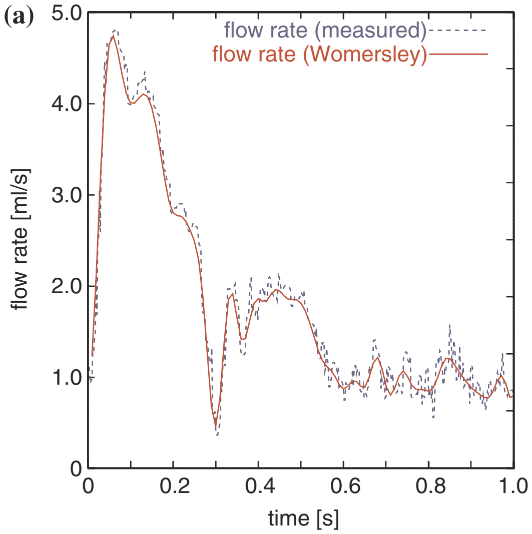

Flowrate waveform.

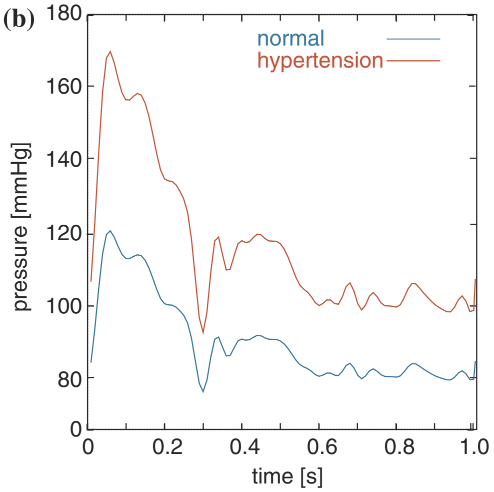

Pressure waveform.

Fig. 2 Transient behavior of the boundary conditions

5 Results

5.1 Wall displacement

Figure 3 shows snapshots of the displacement distributions at the peak systole. For both the NBP and HBP cases the maximum displacement occurs at the aneurysmal wall. The magnitude of the maximum displacement is 0.700 mm for

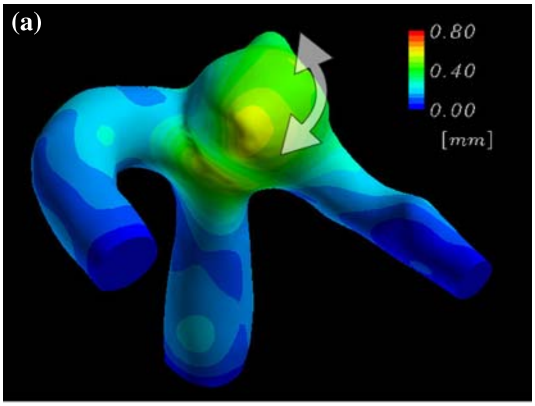

NBP case.

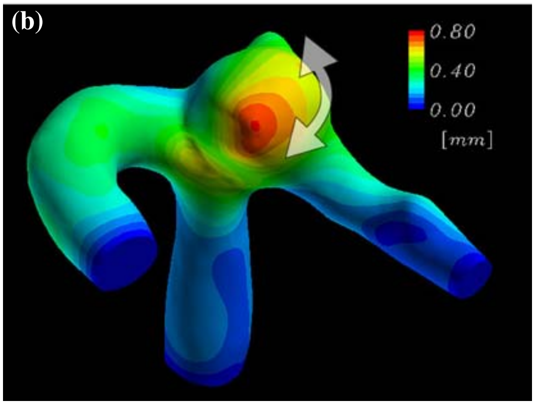

HBP case.

Fig. 3 Instantaneous displacement distribution at the peak systole

the NBP case and 0.752 mm for the HBP case, which are approximately 24% of the arterial diameter and 14% of the aneurysm diameter. In addition to expansion and contraction due to the blood pressure variations, in both cases the aneurysm exhibits a rotating motion (illustrated with the arrows in the figures).

5.2 Wall shear stress

Figure 4 shows the transient behavior of the WSS distributions. The maximum WSS magnitude is 334 dyn/cm^2 for the NBP case, 398 dyn/cm^2 for the HBP case, and 427 dyn/cm^2 for the rigid-wall case. The maximum-WSS location is indicated with a white arrow in the figures. In all cases, the maximum-WSS location is near the root of the aneurysm, which is called the "neck". The maximum WSS occurs immediately after the peak systole for the NBP case, 0.05 s after the peak systole for the HBP case, and at the peak systole for the rigid-wall case. At the beginning of the systole, the WSS magnitude at the neck is 114, 116 and 103 dyn/cm^2, for the NBP, HBP and rigid-wall cases, respectively. The WSS abruptly increases during the systolic period in all cases, and the magnitude of the systolic WSS variation for the HBP case, 282 dyn/cm^2, is 28% larger than that for the NBP case, 220 dyn/cm^2. As previously reported in [31], because of the deformation of the arterial wall, the maximum WSS for the NBP case is less than that for the rigid-wall case. The maximum WSS for the HBP case on the other hand is almost as large as that for the rigid-wall case. Furthermore, a wide region with large WSS magnitude is seen on the aneurysmal wall in the HBP case.

5.3 Interaction between the arterial wall and blood flow

The differences in the WSS distribution are caused by the differences in the interaction between the arterial wall motion and blood flow. The flow-velocity distributions are shown in Fig. 5. The colors depict the velocity magnitude and the vectors are the velocity vectors projected on to the viewing plane. Since the arterial bifurcation is Y-shaped, in all cases the flow coming from the inlet impinges on the arterial wall near the neck. Consequently, the flow velocity and velocity gradient near the wall of the neck are considerably large. Therefore the maximum WSS occurs near the neck. With the expanding motion of the arterial wall in the systolic period, the wall around the flow-impingement region moves away from the impinging flow. Additionally, the expanding motion of the artery upstream of the bifurcation lowers the magnitude of the impinging flow velocity to maintain the flow rate the same. Consequently, the velocity gradient near the impingement region and the resulting WSS are smaller for the elastic-wall cases. At the peak systole, due to the interaction mechanism, the WSS magnitude and impinging-flow velocity for the HBP case are smallest while those for the rigid-wall case are the largest . After the peak systole the WSS magnitude does not decrease for the HBP case although the blood-flow velocity decreases. In fact, the WSS increases and the magnitude exceeds that for the NBP case. After the peak systole, the arterial wall starts contracting due to the decreasing blood pressure, and the wall moves toward the impinging blood flow. Hence the arterial motion enhances the blood flow impingement after the peak systole contrary to what happens before the peak systole. The change in the interaction mechanism at the peak systole is significant especially for the HBP case because the more the arterial wall expands at the peak systole the more it contracts afterwards. As shown in Fig. 5, the blood flow, which has a significant velocity magnitude, is divided at the neck. For the NBP and rigid-wall cases the flow going into the left branch has a rather large velocity magnitude. For the HBP case, on the other hand, the velocity magnitude for the flow going into the left branch is remarkably small, and a flow with large velocity magnitude enters the aneurysm at the peak systole. Because the open mouth of the aneurysm becomes larger, for the HBP case the blood flow tends to enter the aneurysm after the impingement . The flow with large velocity magnitude that enters the aneurysm at the peak systole, with the help of the contracting motion of the aneurysmal wall, runs through near the aneurysmal wall after the peak systole. Therefore, for the the HBP case the velocity gradient near the aneurysmal wall and the resulting

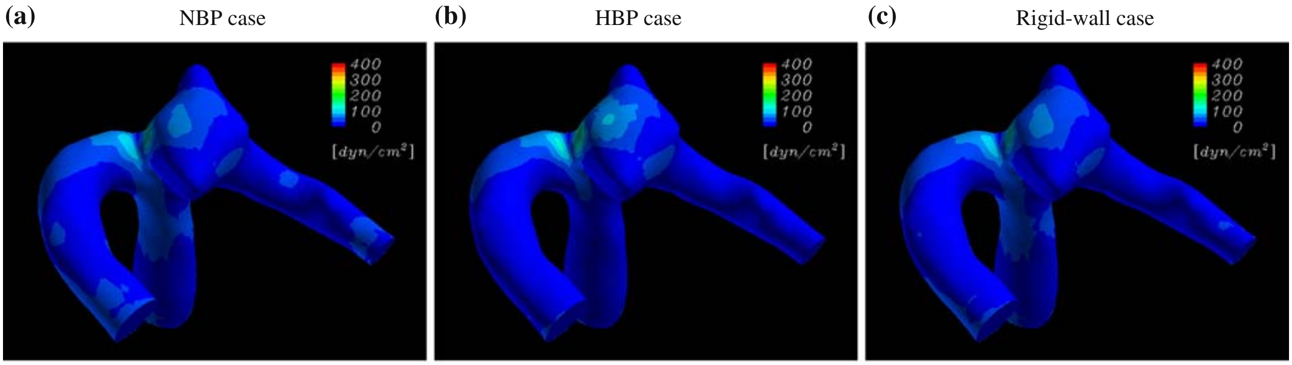
(a) NBP case **(b)** HBP case **(c)** Rigid-wall case

Beginning of the systole (t = 0.01 s).

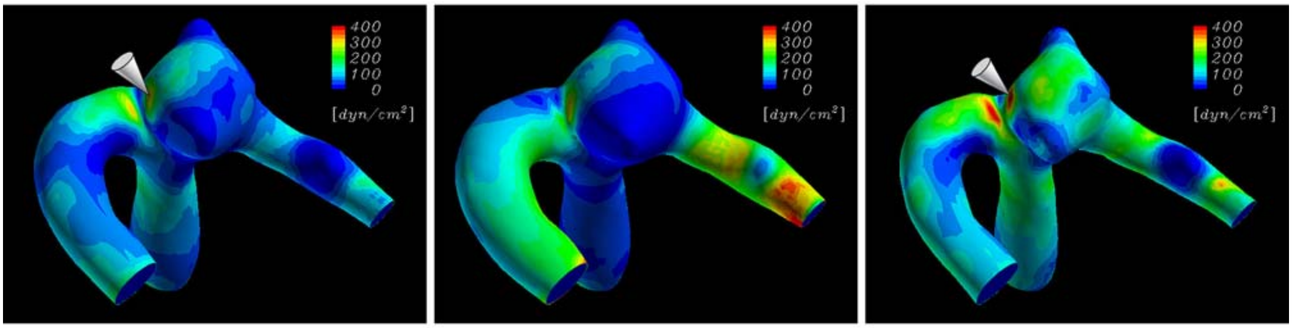

At the peak systole (t = 0.06 s).

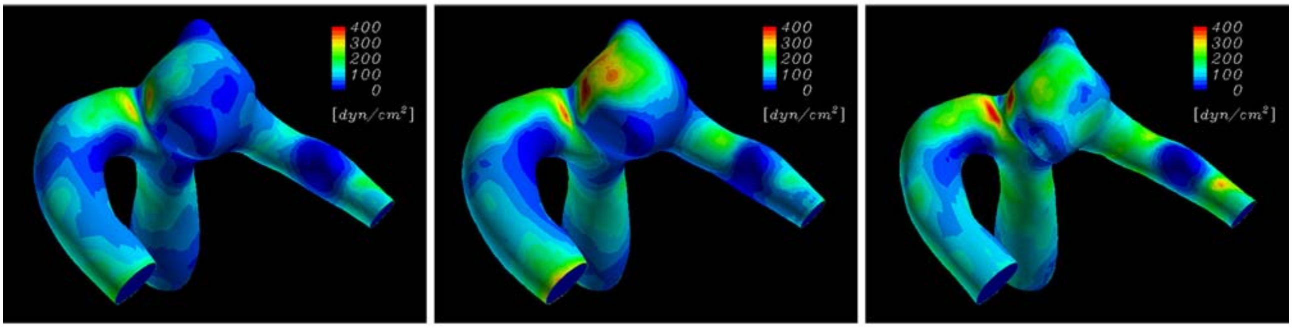

Immediately after the peak systole (t = 0.07 s).

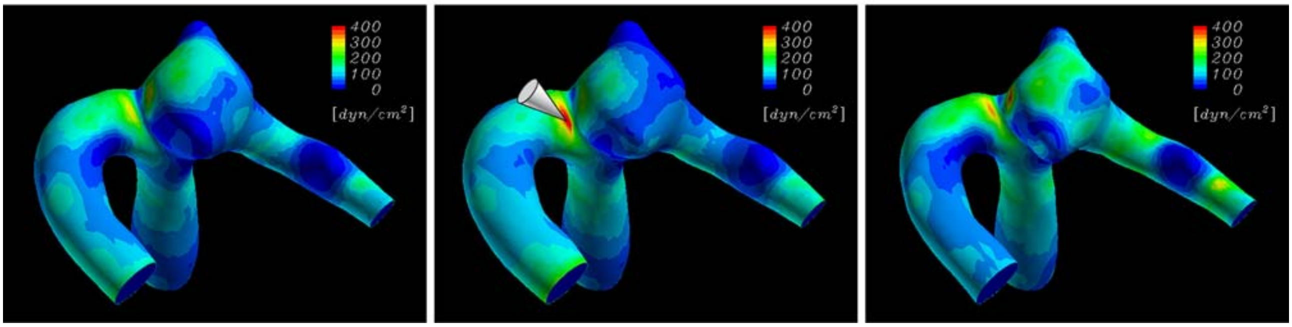

After the peak systole (t = 0.11 s)

Fig. 4 Instantaneous WSS distributions

WSS become considerably large after the peak systole. The interaction mechanism is summarized in Fig. 6.

It is known that high WSS acts on the vascular endothelium as a biological stimulator that modulates the cellular function of the endothelium. Thus, WSS changes due to hypertension possibly cause changes in cellular function in the aneurysmal wall. In the Y-shaped junction we investigate here, the impingement region for the blood flow is near the

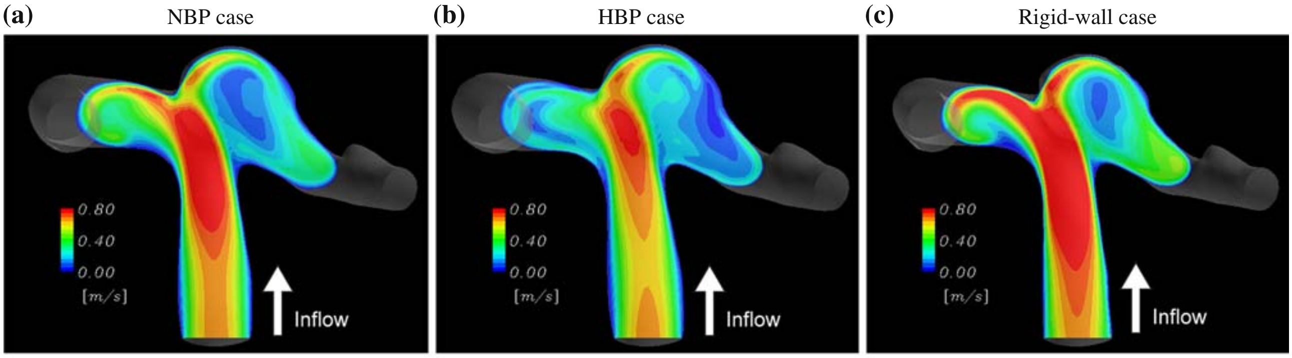

At the peak systole, global view (t = 0.06 s).

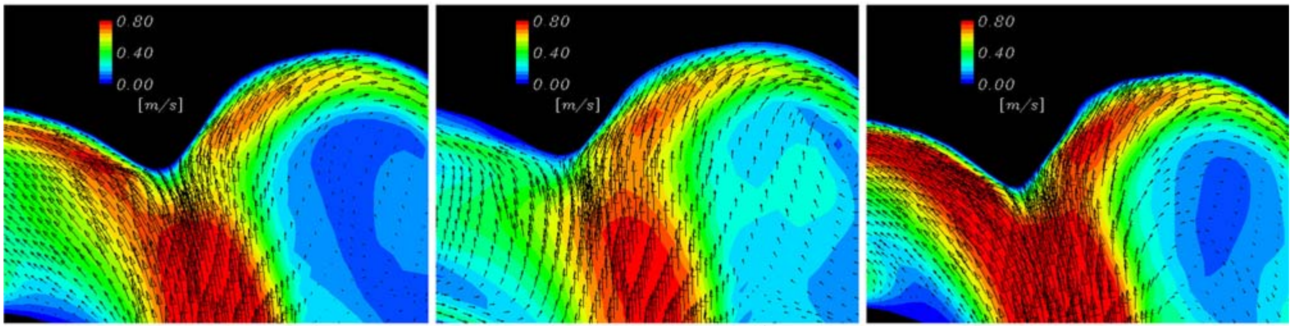

At the peak systole (t = 0.06 s).

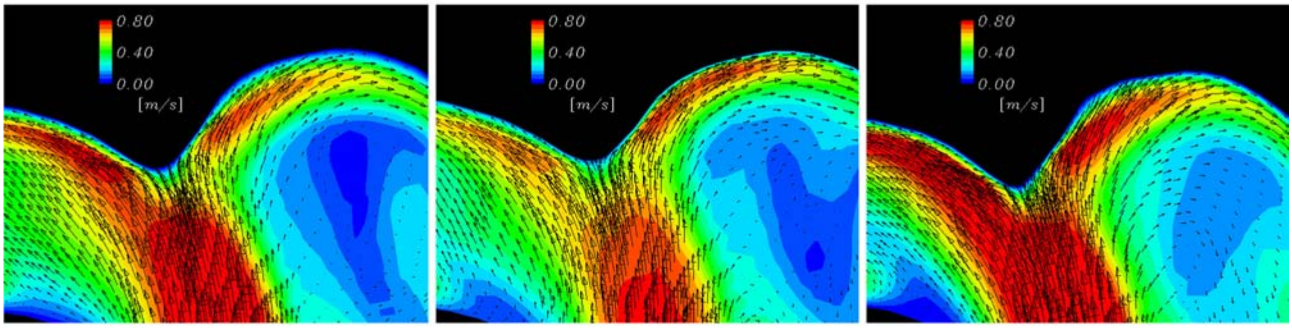

Immediately after the peak systole (t = 0.07 s).

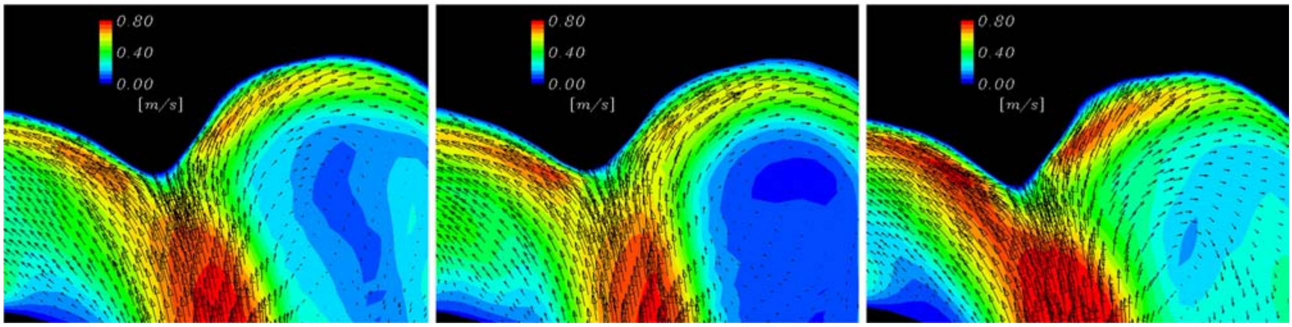

After the peak systole (t = 0.11 s).

Fig. 5 Instantaneous flow-velocity profiles

neck and the hemodynamics in the artery is significantly sensitive to the impingement location. Therefore the dependence of the interaction between the blood flow and the arterial wall on the blood pressure can clearly be seen. As the next step, we plan to investigate for various arterial geometries the effect of hypertension in general.

5.4 Mechanical stress in the arterial wall

Figure 7 shows the instantaneous principal-stress distributions for the luminal wall of the artery. For both the NBP and HBP cases the maximum principal stress occurs at the peak systole and has a value of 690 and 1080 kPa, respectively. The maximum principal stress occurs near the neck as indicated with the white arrow. The comparison of the principal stress distributions at the beginning of the systole and at the peak systole shows that the systolic variation of the principal stress is considerably large, similar to what we observed for the WSS. The maximum principal stress at the beginning of the systole is 84.6 and 152 kPa for the NBP and HBP cases. The magnitude of the variation in the principal stress during the systolic period is 605 and 928 kPa for the NBP and HBP cases. Although both the maximum value and maximum variation of the principal stress occur around the neck for both the NBP and HBP cases, we consider the principal stress in the aneurysmal wall also to be important because that is where the aneurysm tends to rupture. The maximum value and variation of the principal stress in the aneurysmal wall occurs at the point indicated in the figure with the yellow arrow. For both the NBP and HBP cases, that location is near the part called the "bleb", which is a small saccular aneurysm on the aneurysmal wall. The existence of a bleb is one of the known indicators in rupture-risk estimation. The maximum principal stress in the aneurysmal wall is 212 and 310 kPa for the NBP and HBP cases. The systolic variation of the principal stress is 183 and 249 kPa for the NBP and HBP cases. The maximum value and variation of the principal stress for the HBP case are approximately 50% larger than those for the NBP case, although the maximum displacement is only 7% larger. This is because the structure of the arterial wall is complicated particularly near the aneurysm.

These results show that hypertension also significantly affects the stress distribution in the arterial walls. In fact, the wall thickness for the aneurysmal wall is smaller than 0.3 mm, which is what we assumed in this study. Therefore the magnitude of the mechanical stress in the aneurysmal wall should be larger than what we find in this study. Although the mechanism of the rupture in cerebral aneurysm needs further investigation, these results show that hypertension could enhance the damage in arterial wall tissue in terms of structural mechanics.

6 Conclusions

We computed the cardiovascular fluid–structure interactions of aneurysmal conditions with high and normal blood pressures. This demonstrates the potential of image-based FSI modeling in disease simulation and in investigating the effect of hypertension on the cerebral aneurysm.

The results show that hypertensive blood pressure causes significant changes in the WSS distribution on the aneurysmal wall and in the stress distribution in the aneurysmal wall. This implies that hypertension possibly affects the growth of aneurysm and leads to damage in the aneurysmal wall. Although the mechanisms for how a cerebral aneurysm initiates, grows and ruptures still remain to be investigated, we consider the blood pressure to be an important factor in cerebral aneurysm. We are planning to further investigate the effect of hypertension on the aneurysm by using various arterial geometries. We are also planning to, by using the Windkessel model, take into account the phase lag between the velocity and pressure waveforms, since in our current study these two are assumed to vary in the same phase.

Other known risk factors such as smoking can also affect the hemodynamics through the variation in the heart beat rate, the blood pressure or the arterial impedance. We believe that those risk factors can be incorporated into our modeling in the same way as we have incorporated hypertension. The current study shows the potential for image-based FSI modeling to be used in the future as a disease simulator.

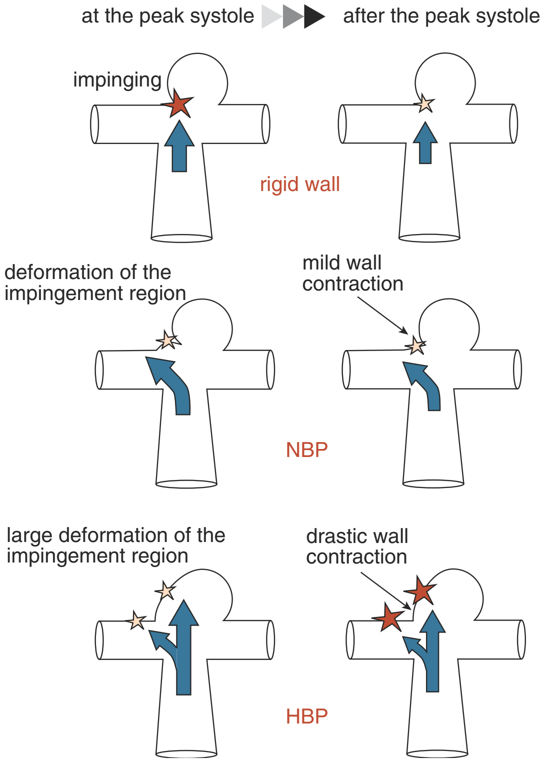

Fig. 6 Interaction between the blood flow and the arterial wall

Acknowledgements Authors would be grateful to Dr. Motoharu Hayakawa, Fujita Health University (Aichi, Japan) for providing CT and for his suggestions in terms of radiology. Authors also acknowledge Toshiba Medical, Inc., for providing image processing software ALATOVIEW. Part of this research was carried out within the framework of the project "Frontier Simulation Software for Industrial Science (FSIS)", supported by the IT program of the Ministry of Education, Culture, Sports, Science and Technology (MEXT).

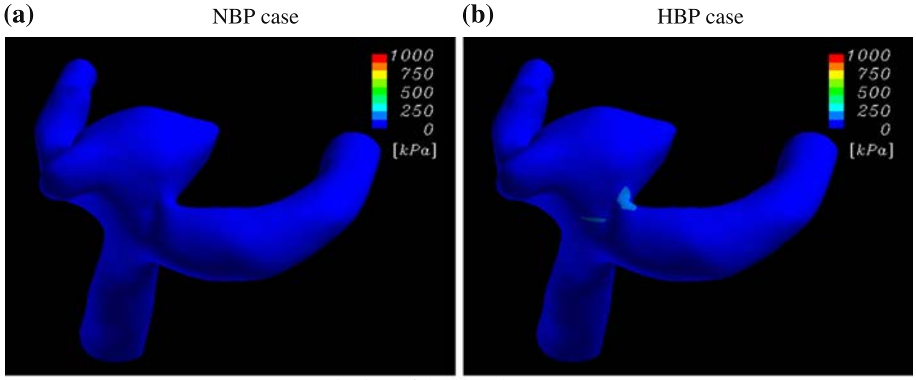
(a) NBP case **(b)** HBP case

Beginning of the systole (t = 0.01 s).

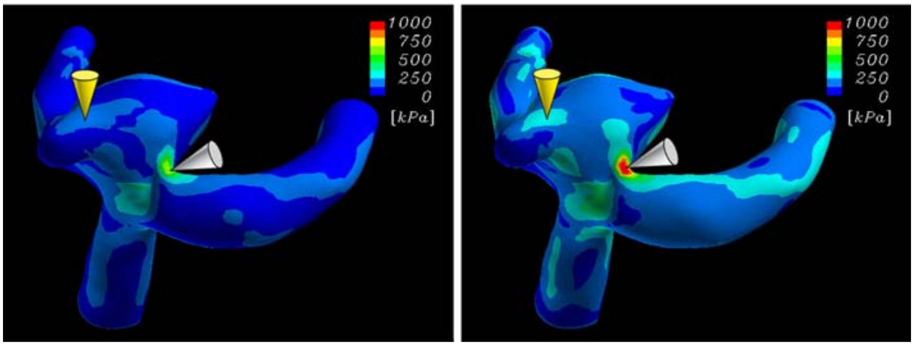

At the peak systole (t = 0.06 s).

Fig. 7 Instantaneous principal-stress distributions

References

1. Asakura T, Karino T (1990) Flow patterns and spatial distribution of atherosclerotic lesions in human coronary arteries. Circ Res 66:1045–1066
2. Brooks AN, Hughes TJR (1982) Streamline upwind/Petrov-Galerkin formulations for convection dominated flows with particular emphasis on the incompressible Navier-Stokes equations. Comput Method Appl Mech Eng 32:199–259
3. Caro CG, Fitz-Gerald JM, Schroter RC (1971) Atheroma arterial wall shear-observation, correlation and proposal of a shear dependent mass transfer mechanism for atherogenesis. Proc R Soc Lond (Biol) 177:109–159
4. Johnson AA, Tezduyar TE (1994) Mesh update strategies in parallel finite element computations of flow problems with moving boundaries and interfaces. Comput Method Appl Mech Eng 119:73–94
5. Kaazempur-Mofrad MR, Ethier CR (2001) Mass transport in an anatomically realistic human right coronary artery. Ann Biomed Eng 29(2):121–127
6. Karino T, Takeuchi S, Kobayashi N, Motomiya M, Mabuchi S (1993) Fluid dynamics of cerebrovascular disease (in Japanese). Neurosurgeons 12:15–24
7. Komatsu Y, Yasuda S, Shibata T, Ono Y, Hyodo A, Nose T (1994) Management for subarachnoid hemorrhage with negative initial angiography. Neurol Surg (in Japanese) 22:43–49
8. Loremson WE, Cline HE (1987) Marching Cubes: a high resolution 3D surface construction algorithm. Comput Graphics 21(4):163–169
9. Malek AM, Alper SL, Izumo S (1999) Hemodynamic shear stress and its role in atherosclerosis. J Am Med Assoc 282:2035–2042
10. McDonald DA (1974) Blood flow in arteries, 2nd edn. Edward Arnold
11. Oshima M, Torii R, Kobayashi T (2004) Simulation of blood flow in the cerebral arterial circle of Willis. In: Proceedings of WCCM6, ICCM, Beijing, China, pp CD-ROM
12. Prosi M, Zunino P, Perktold K, Quarteroni A (2005) Mathematical and numerical models for transfer of low-density lipoproteins through the arterial walls: a new methodology for the model set up with applications to the study of disturbed lumenal flow. J Biomech 38(4):903–917
13. Raghavan ML, Vorp DA, Federie MP, Makaroun MS, Webster MW (2000) Wall stress distribution on three-dimensionally reconstructed models of human abdominal aortic aneurysm. J Vasc Surg 31(4):760–769
14. Santamarina A, Weydahl E, Siegel JM, Moore JE (1998) Computational analysis of flow in a curved tube model of the coronary arteries: Effects of time-varying curvature. Ann Biomed Eng 26(6):944–954
15. Steiger HJ (1990) Pathophysiology of development and rupture of cerebral aneurysms. Acta Neurochir Suppl 48:1–57
16. Stein K, Benney R, Kalro V, Tezduyar TE, Leonard J, Accorsi M (2000) Parachute fluid–structure interactions: 3-D Computation. Comput Method Appl Mech Eng 190:373–386
17. Stein K, Benney R, Tezduyar T, Potvin J (2001) Fluid–structure interactions of a cross parachute: numerical simulation. Comput Method Appl Mech Eng 191:673–687
18. Stein KR, Benney RJ, Tezduyar TE, Leonard JW, Accorsi ML (2001) Fluid–structure interactions of a round parachute: Modeling and simulation techniques. J Aircraft 38:800–808
19. Steinman DA (2002) Image-based computational fluid dynamics modeling in realistic arterial geometries. Ann Biomed Eng 30:483–497
20. Tang D, Yang C, Kobayashi S, Zheng J, Vito RP (2003) Effect of stenosis asymmetry on blood flow and artery compression: a three dimensional fluid-structure interaction model. Ann Biomed Eng 31(10):1182–1193

21. Taylor CL, Yuan Z, Selman WR, Ratcheson RA, Rimm AA (1995) Cerebral arterial aneurysm formation and rupture in 20,767 elderly patients: hypertension and other risk factors. J Neurosurg 83:812–819
22. Tezduyar TE (1992) Stabilized finite element formulations for incompressible flow computations. Advances in Applied Mechanics 28:1–44
23. Tezduyar TE (2001) Finite element methods for flow problems with moving boundaries and interfaces. Arch Comput Method Eng 8:83–130
24. Tezduyar TE (2004) Finite element methods for fluid dynamics with moving boundaries and interfaces. In: Stein E, Borst RD, Hughes T (eds) Encyclopedia of Computational Mechanics, Volume 3: Fluids, Wiley, New York, chap 17
25. Tezduyar TE, Behr M, Liou J (1992) A new strategy for finite element computations involving moving boundaries and interfaces – the deforming-spatial-domain/space–time procedure: I. The concept and the preliminary numerical tests. Comput Method Appl Mech Eng 94(3):339–351
26. Tezduyar TE, Behr M, Mittal S, Johnson AA (1992) Computation of unsteady incompressible flows with the finite element methods – space–time formulations, iterative strategies and massively parallel implementations. In: New methods in transient analysis, ASME, New York, PVP-Vol.246/AMD-Vol.143, pp 7–24
27. Tezduyar TE, Behr M, Mittal S, Liou J (1992) A new strategy for finite element computations involving moving boundaries and interfaces – the deforming-spatial-domain/space–time procedure: II. Computation of free-surface flows, two-liquid flows, and flows with drifting cylinders. Comput Method Appl Mech Eng 94(3): 353–371
28. Tezduyar TE, Mittal S, Ray SE, Shih R (1992) Incompressible flow computations with stabilized bilinear and linear equal-order-interpolation velocity-pressure elements. Comput Method Appl Mech Eng 95:221–242
29. Torii R, Oshima M, Kobayashi T, Takagi K (2001) Numerical simulation system for blood flow in the cerebral artery using CT imaging data. JSME Int J, Series C 44(4):982–989
30. Torii R, Oshima M, Kobayashi T, Takagi K, Tezduyar TE (2006) Computer modeling of cardiovascular fluid-structure interactions with the deforming-spatial-domain/stabilized space-time formulation. Comput Method Appl Mech Eng 195:1885–1895
31. Torii R, Oshima M, Kobayashi T, Takagi K, Tezduyar TE (2006) Influence of wall elasticity in patient-specific hemodynamic simulations. Comput Fluids published online
32. Vorp DA, Vande Geest JP (2005) Biomechanical determinants of abdominal aortic aneurysm rupture. Arterioscl Throm Vas Biol 25(8):1558–1566
33. Wan J, Steele B, Spicer SA, Strohband S, Feijoo GR, Hughes TJR, Taylor CA (2002) A one-dimensional finite element method for simulation-based medical planning for cardiovascular disease. Comput Method Biomech Biomed Eng 5(3):195–206
34. Womersley JR (1955) Method for the calculation of velocity, rate of flow and viscos drag in arteries when the pressure gradient is known. J Physiol 127:553–563
35. Zarins CK, Zatina MA, Giddens DP, Ku DN, Glagov S (1987) Shear stress regulation of artery lumen diameter in experimental atherogenesis. J Vas Surg 5(3):413–420
36. Zeng D, Ding Z, Friedman MH, Ethier CR (2003) Effects of cardiac motion on right coronary artery hemodynamics. Ann Biomed Eng 31(4):420–429